Origins of Life

International Edition: DOI: 10.1002/anie.201610781
German Edition: DOI: 10.1002/ange.201610781

Steep pH Gradients and Directed Colloid Transport in a Microfluidic Alkaline Hydrothermal Pore

*Friederike M. Möller, Franziska Kriegel, Michael Kieß, Victor Sojo, and Dieter Braun**

Abstract: *All life on earth depends on the generation and exploitation of ionic and pH gradients across membranes. One theory for the origin of life proposes that geological pH gradients were the prebiotic ancestors of these cellular disequilibria. With an alkaline interior and acidic exterior, alkaline vents match the topology of modern cells, but it remains unknown whether the steep pH gradients persist at the microscopic scale. Herein, we demonstrate the existence of 6 pH-unit gradients across micrometer scales in a microfluidic vent replicate. Precipitation of metal sulfides at the interface strengthens the gradients, but even in the absence of precipitates laminar flow sustains the disequilibria. The gradients drive directed transport at the fluid interface, leading to colloid accumulation or depletion. Our results confirm that alkaline vents can provide an exploitable pH gradient, supporting their potential role at the emergence of chemiosmosis and the origin of life.*

In modern cells, pH and ionic gradients across nanometer-thick phospholipid membranes drive energy conversion and storage. This "chemiosmotic coupling" is ubiquitous to all branches of life and points towards an early emergence during evolution. On the early Earth, alkaline hydrothermal vent systems offered rich geochemical and physical far-from-equilibrium conditions with striking resemblances to modern biology.[1] The interface between the Hadean ocean and the alkaline effluent naturally provided steep gradients of temperature, pH, ion concentration, osmotic pressure, and redox and electric potentials.[2] Precipitation reactions further created microporous networks of catalytic metal–sulfur precipitates. These have been hypothesized to represent rudimentary inorganic analogues to modern phospholipid membranes, and seem to be poised to drive early carbon and energy metabolisms.[3]

Sharp liquid interfaces are typically not stable due to elution by diffusion. Mechanisms for the stabilization and steepening of concentration gradients are thus required for the evolution of functional membranes. We show that precipitation reactions and hydrodynamic flows can readily serve this purpose. Previous studies have shown that chemical garden structures can maintain pH gradients for several hours.[4,5] However, the macroscopic nature of these experiments could not assess the steepness of the gradient. Herein, we apply fluorescence microscopy to measure the pH distribution in a microfluidic vent replica on the microscale.

Besides powering (bio-)chemical processes, such as redox reactions for carbon fixation, ion gradients can also induce directed colloid transport. The transport in chemical potential gradients has been known as diffusiophoresis since 1947,[6] but has historically received scant attention in the literature. Only recently has it regained attention in diverse research fields, for example in material sciences[7] and microfluidic lab-on-a-chip technologies.[8–10] Furthermore, it has been shown that diffusiophoresis can enhance DNA translocation through nanopores,[11,12] and drive bacterial chemotaxis[13] and self-propelling devices.[14,15]

The coupling of physical transport in far-from-equilibrium settings has already led to the discovery of phenomena in the origin-of-life context. For example, temperature gradients were exploited to trigger essential aspects of basic Darwinian evolution, such as accumulation,[20] polymerization by hybridization,[21] replication,[22] and selection[23] of DNA. Here, we applied fluorescence microscopy to monitor diffusiophoresis of fluorescent microspheres and developed a finite-element model to explain our experimental results.

In our experiments, two high-precision syringe pumps ensure a reproducible laminar co-flow of two solutions with sustained pH and ionic gradients. To reduce the complexity of the system and to exclude side effects due to buffering or redox reactions, we used pure Na_2S (10 mM, pH 11.8) and $FeCl_2$ (10 mM, pH 5.8) solutions to emulate the hydrothermal effluent and the Hadean ocean. A solid barrier forms at the confluence of the two solutions (Figure 1). A full microscopy movie of the precipitation process is provided in the Supporting Information. First, a thin, smooth barrier forms. Later, the barrier thickens and a granular structure develops at the ocean-facing side. This behavior suggests the existence of a compositional gradient across the barrier in accordance with the literature, which provides detailed structural analyses of similar precipitates.[5,16–19] All of the experiments were performed under anoxic conditions to simulate the situation on the early Earth. Thus, the precipitates are expected to mainly include FeS and $Fe(OH)_2$. Both salts have rich chemistries that involve multiple transformations into each other as well as other salts, such as Fe_3S_4, Fe_3O_4, and FeS_2, with significant consequences for geochemistry and geochemically powered catalysis.[19,24] The pH distribution within the microfluidic flow cell was imaged with micrometer resolution using the ratiometric, pH-dependent fluorescence of SNARF1. The stability of the pH gradient against diffusion was tested by stepwise reduction of the inflow rate (Figure 2a). To elucidate

[*] F. M. Möller, F. Kriegel, M. Kieß, Dr. V. Sojo, Prof. D. Braun
Systems Biophysics, Physics Department
Nanosystems Initiative Munich and Center for NanoScience
Ludwig-Maximilians-Universität München
Amalienstraße 54, 80799 München (Germany)
E-mail: dieter.braun@lmu.de

Supporting information for this article can be found under: http://dx.doi.org/10.1002/anie.201610781.

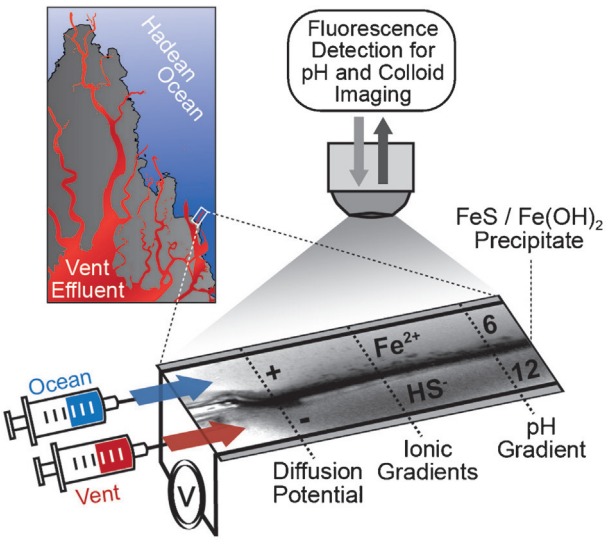

Figure 1. Sketch of a hydrothermal vent chimney and the experimental setup. Syringe pumps ensure reproducible laminar flow conditions, sustained gradients, and defined precipitation at the fluid interface between the minimally emulated hydrothermal effluent and Hadean ocean in a glass capillary dimensions of 3 mm × 3 cm, with a depth of 300 µm (not shown). Platinum electrodes allow measuring the electric potential across the chamber. The fluorescence image is taken at the end of a typical experiment and shows the darkening of fluorescence by the precipitate at the fluid interface. Being smooth on the hydrothermal interface and granular at the ocean interface, the structure of the precipitate indicates a compositional gradient in accordance with the literature.[5,16–19]

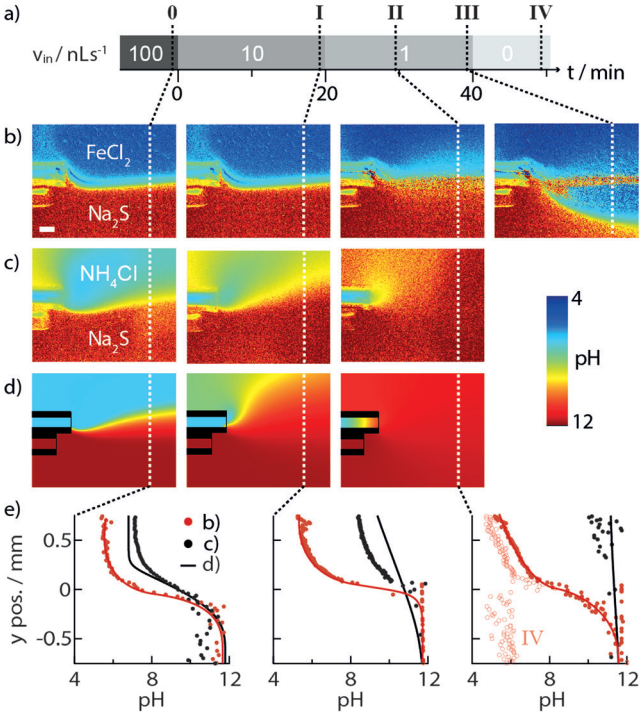

Figure 2. Stability of the pH gradient. a) The inflow rate is stepwise reduced to test the stability of the pH gradient. b) With precipitation, a steep and stable pH gradient built up. The relaxation of the gradient only sets in 600 s after the slowdown to 1 nL s^{-1}. Scale bar = 200 µm. Without precipitation, a less stable pH gradient was observed in c) experiment and d) simulation. e) pH profiles along the dashed, white cut lines in panels (b–d). The solid red line is drawn to guide the eye.

the role of precipitation, control experiments were performed, in which the $FeCl_2$ solution was substituted by a non-precipitate-forming NH_4Cl solution (10 mM, pH 6.8). Details on the microfluidic design, the optical setup, and experimental methods for sample preparation, image analysis, and ratiometric pH imaging are provided in the Supporting Information.

The experimental pH images (Figure 2b) reveal that the initial difference of 6 pH units between the $FeCl_2$ and the Na_2S solution is maintained for inflow rates of 100 nL s^{-1} and 10 nL s^{-1} with a gradient of approximately 0.024 pH units per µm at 1 mm distance from the inlets. Even when the flow rate is reduced to 1 nL s^{-1}, the gradient is still stable for several hundred seconds before a slow relaxation sets in. In the control experiment without precipitation, diffusion attenuates the gradient even at high inflow rates, and a diminished maximum gradient of 0.01 pH units per µm is observed (Figure 2c). The agreement with finite-element simulations (Figure 2d) confirms that this experiment is fully described by hydrodynamics, diffusion, and the acid-base equilibrium of ammonium. The initial H^+ concentration in the flow chamber is negligible, owing to the logarithmic nature of the pH scale and a near-neutral starting pH of the ocean solution. Thus, pH dynamics are mainly driven by OH^- diffusion leading to an alkaline final pH. In contrast, the final pH with precipitation is acidic, as OH^- is consumed by the precipitation reactions. A detailed description of the model can be found in the Supporting Information. In experiment and simulation, a new steady-state pH distribution is established within a few seconds after each flow rate reduction step. In contrast, the final relaxation of the pH gradient in the experiment with precipitation requires several tens of minutes. This points towards a reaction-controlled rather than diffusion-controlled process, limited by the depletion of precipitation resources. The final relaxation further implies that the ongoing precipitation reactions, and not the barrier itself, stabilize the pH gradient. Thus, the fluid interface facilitates steep gradients without being completely impermeable to ions. Leakiness of barriers is considered an important feature for early life to avoid chemical equilibrium before an active pumping machinery had evolved.[25]

The sharp ionic gradients at vent-ocean interfaces suggest diffusiophoresis to be an important phenomenon. Diffusiophoresis describes the directed transport of colloids in salt gradients driven by osmotic pressure p_{osm} (chemiphoresis) and spontaneously emerging electric fields $\boldsymbol{E}_{diff}$ (electrophoresis). Chemiphoresis typically transports colloids along ionic strength gradients per $\boldsymbol{v}_{osm} = D_{DP}^{osm} \nabla \log(I)$, where I is the ionic strength and D_{DP}^{osm} is the colloid's osmotic diffusiophoretic coefficient. This parameter is very sensitive to the ionic environment and its prediction for arbitrary electrolytes is not possible.[26] The different diffusion coefficients of the individual ionic species further lead to the generation of an electric field $\boldsymbol{E}_{diff}$ in free solution, which transports colloids according

to their electrophoretic mobility μ with $\boldsymbol{v}_{el} = \mu\, \boldsymbol{E}_{diff}$. Following the derivation procedure by Chiang et al.,[27] an expression for $\boldsymbol{E}_{diff}$ was derived (Supporting Information) that depends on the individual ion concentrations c_i, the ion diffusion coefficients D_i, the ion valences z_i, and on the hydrodynamic velocity $\boldsymbol{v}_{HD}$:

$$\boldsymbol{E}_{diff} = \frac{k_B T}{e} \frac{\sum_i z_i (D_i \nabla c_i - \boldsymbol{v}_{HD} c_i)}{\sum_i z_i^2 D_i c_i} \quad (1)$$

Here, we used negatively charged, fluorescently labeled polystyrene microspheres to observe colloid transport in the microfluidic vent replica. The single particle time traces report on the superposition of the hydrodynamic laminar flow $\boldsymbol{v}_{HD}$ and diffusiophoretic transport $\boldsymbol{v}_{DP} = \boldsymbol{v}_{el} + \boldsymbol{v}_{osm}$, and reveal coupling phenomena both with and without precipitation.

Figure 3a sketches the situation in a typical experiment with precipitation. The hydrodynamic co-flow of contrasting solutions creates steep ionic gradients. The precipitation reactions locally decrease the ionic strength and generate an osmotic force away from the fluid interface. On the other hand, the differential diffusion of ions and the ion-exchanging iron sulfide precipitation give rise to electric forces. The hydrodynamic streamlines in Figure 3b were simulated by solving the Navier–Stokes equation using finite-element methods. In a control experiment without solute contrast, no deviation of the colloid transport from the hydrodynamic finite-element simulation became apparent (Figure S3).

In the experiment with solute contrast and precipitation, the colloid transport in bulk solution at 10 nL s^{-1} inflow rate was still mainly governed by hydrodynamics. However, adjacent to the precipitated barrier, a colloid-free zone formed (Figure 3c). A similar effect has been observed before at ion-exchange membranes by Florea et al.[7] For explanation, they established a theory based on the combination of ion exchange reactions and diffusiophoresis, which supports the model sketched in Figure 3a. Immediately after slowing down to 1 nL s^{-1}, strongly enhanced lateral migration towards the ocean was observed and colloid entry from the ocean reservoir was fully suppressed. The pH gradient was still stable at this point (Figure 2a), and thus the effect must be driven by other ions. It would be desirable to explicitly model the ion distributions within the flow cell to understand these phenomena. However, missing quantitative data on precipitation kinetics, and on other properties, such as ion binding capabilities of the precipitate, render this impossible without an excessive number of free parameters.

In contrast, the ion distributions in the experiment without precipitation can be fully simulated by a time-dependent finite-element model, considering hydrodynamics, diffusion, and acid–base equilibria. This allows us to infer the electric field per Equation (1) and the spatiotemporally resolved colloid velocity $\boldsymbol{v}_{coll} = \boldsymbol{v}_{HD} + \boldsymbol{v}_{DP}$. In the experiment, accumulation of colloids at the fluid interface was observed at 10 nL s^{-1} inflow rate (Figure 4a). Upon slowdown, a similar behavior to that with precipitation was observed; lateral migration set in and colloid inflow from the ocean reservoir was hindered (Figure 4b). The simulations nicely reproduce all of the observations. The properties of the colloid were used as fit parameters, and the best agreement was found for $\mu = -9.28 \times 10^{-8}$ µm^2 V^{-1} s^{-1} and $D_{DP}^{osm} = 0$ µm^2 s^{-1}. This implies that electrophoresis is the major driving force, which is also supported by the occurrence of electric potentials

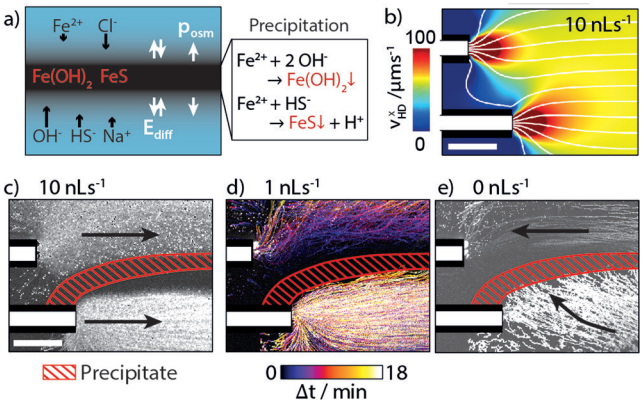

Figure 3. Colloid transport with precipitation. The upper inflow delivers $FeCl_2$ and the lower one Na_2S. a) Differential ion diffusion (black arrows) generates an electric field at the interface. The precipitation reactions locally decrease the ionic strength and cause an osmotic pressure. b) Simulated hydrodynamic flow. The shape of the streamlines is independent of the inflow rate and the amplitude scales linearly. c–e) Experimental colloid transport. c) The average fluorescence intensity of 100 frames (500 s) in steady state reveals a colloid-free zone adjacent to the precipitated barrier. d) Time-dependent migration towards the ocean after slowdown. e) Without inflow, reverse flows towards the ocean inlet occur. Scale bars = 500 µm.

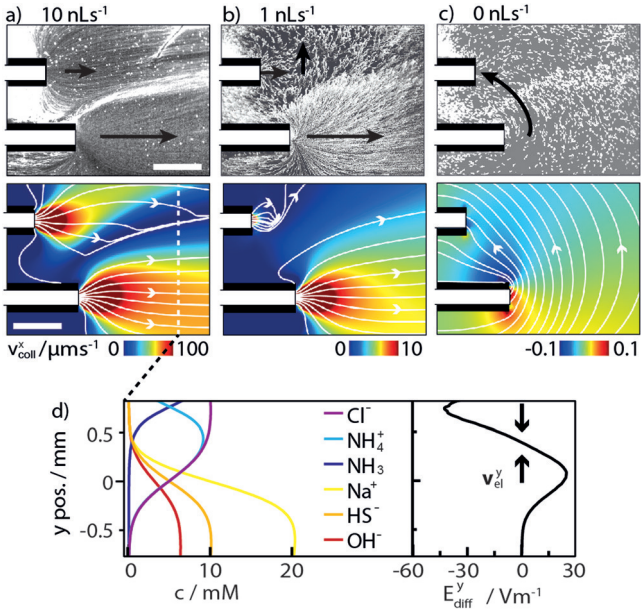

Figure 4. Colloid transport without precipitation. Comparison of experiment and simulation. The upper inflow delivers NH_4Cl and the lower one Na_2S. Scale bars = 500 µm. a) At 10 nL s^{-1} inflow rate, colloid accumulation at the fluid interface was observed. b) Upon slowdown, colloid inflow on the ocean side was suppressed. c) Without inflow, reversed transport towards the ocean inlet occurred. d) Simulated ion distribution and consequential electric field per Equation (1) at 10 nL s^{-1} inflow rate 1 mm behind the inlet (dashed line).

between the two platinum electrodes in the microfluidic flow chamber. (See Figure S5 for detailed results).

To illustrate the electric field generation mechanism, the simulated ion distributions at 10 $nL\,s^{-1}$ at 1 mm distance from the inlet (dashed, white cutline in Figure 4a) and the lateral electric field per Equation (1) are plotted in Figure 4d. The black arrows indicate the focusing electric force on negatively charged colloids. The individual ion contributions to Equation (1) reveal that the focusing is caused by chloride and ammonium buffer ions, while the overall drift towards the ocean is driven by sodium and chloride (Figure S2). This result can explain the lateral migration in the experiment with precipitation and allows the conclusion that the precipitate barrier is widely permeable to these ions.

In summary, we introduced a microfluidic vent replica for the investigation of electrochemical gradients and associated transport processes on the microscale. The method ensures reproducible non-equilibrium conditions for the self-assembly of inorganic barriers in strong ionic gradients. The combination of ratiometric pH imaging, single-particle tracking, electric potential measurements, and kinetic finite-element simulations provides insight into the electro-geochemical processes at the barrier. We found that the precipitation reactions alone stabilize and steepen the pH gradient at the fluid interface. We expect that this effect occurs in a similar fashion for more complex solutions, as long as the pH difference and the required ions (Fe^{2+}, HS^-, OH^-) are present. This is because, as we show, pH stabilization is not a property of the barrier structure, but of the precipitation reaction itself. The reproducibility of the microfluidic approach will allow the targeted optimization of the barrier and the associated disequilibria by adjustment of flow rates and ionic compositions. More realistic mimics of the ancient vent and ocean fluids can be applied, which are expected to contain additional metal ions (for example, Ni^{2+}), high NaCl concentrations, and diverse dissolved gases (such as CO_2, CH_4, and H_2). In this way, the approach can be promoted towards a chemical-flow reactor for the detection of carbon fixation reactions central to the alkaline-vent theory.[1,3,20] In contrast to macroscopic approaches,[20] the microscale nature of the flow chamber prevents dilution of reaction products into the bulk solution. Significantly, the reduction of CO_2 with H_2 at real Fe(Ni)S hydrothermal vent chimneys has been suggested to require an electrochemical overpotential of more than 180 mV, corresponding to a pH gradient of 3 to 4 units.[28] We show such gradient sizes at microscopic scales, promoting potential studies of carbon fixation pathways under alkaline vent conditions.

The observation of diffusiophoresis in the vent system suggests intricate feedback situations. Notably, without tuning of conditions, we observed interesting phenomena such as strong accumulation, enhanced migration of colloids, and the emergence of colloid-free zones. In an additional experiment, shown in Figure S6, we observe the incorporation of fluorescent phospholipid vesicles into the inorganic precipitate. In combination with diffusiophoresis, this observation shows that it is possible to position vesicles within extreme geochemical gradients, which is an interesting setting in the context of early bioenergetics.[25] The results also agree with recent publications regarding the incorporation of proteins[29] into chemical garden structures, and salt-gradient-enhanced particle deposition on microporous membranes.[30]

In conclusion, the presented microfluidic vent replica can serve as a test bed for the investigation of geochemical processes at the microscale, as well as for the discovery of evolutionary pathways from inorganic to biochemically active barriers and the emergence of an ion-gradient-driven early protometabolism.

Acknowledgements

We thank Laura Barge and Michael Russell for sharing their expertise in prebiotic geochemistry and in the preparation of FeS barriers, Dominic Berchthold for preliminary experiments, and Christof Mast and Simon Lanzmich for programming support. Financial support from the Simons Foundation, the Center for NanoScience (CeNS), the Nanosystems Initiative Munich (NIM) and the European Molecular Biology Organization (EMBO, to VS), is gratefully acknowledged.

Conflict of interest

The authors declare no conflict of interest.

Keywords: alkaline vents · diffusiophoresis · molecular electrochemistry · molecular evolution · origin of life

How to cite: *Angew. Chem. Int. Ed.* **2017**, *56*, 2340–2344
Angew. Chem. **2017**, *129*, 2380–2384

[1] W. Martin, M. J. Russell, *Philos. Trans. R. Soc. London Ser. B* **2007**, 362.
[2] K. Zahnle, N. Arndt, C. Cockell, A. Halliday, E. Nisbet, F. Selsis, N. H. Sleep, *Space Sci. Rev.* **2007**, *129*, 35–78.
[3] V. Sojo, B. Herschy, A. Whicher, E. Camprubí, N. Lane, *Astrobiology* **2016**, *16*, 181–197.
[4] L. M. Barge, I. J. Doloboff, L. M. White, G. D. Stucky, M. J. Russell, I. Kanik, *Langmuir* **2012**, *28*, 3714–3721.
[5] F. Glaab, M. Kellermeier, W. Kunz, E. Morallon, J. M. García-Ruiz, *Angew. Chem. Int. Ed.* **2012**, *51*, 4317–4321; *Angew. Chem.* **2012**, *124*, 4393–4397.
[6] B. V. Derjaguin, G. P. Sidorenkov, E. A. Zubashchenkov, E. V. Kiseleva, *Kolloidn. Zh.* **1947**, *9*, 335–347.
[7] D. Florea, S. Musa, J. M. R. Huyghe, H. M. Wyss, *Proc. Natl. Acad. Sci. USA* **2014**, *111*, 6554–6559.
[8] B. Abécassis, C. Cottin-Bizonne, C. Ybert, A. Ajdari, L. Bocquet, *Nat. Mater.* **2008**, *7*, 785–789.
[9] S. Shin, E. Um, B. Sabass, J. T. Ault, M. Rahimi, P. B. Warren, H. A. Stone, *Proc. Natl. Acad. Sci. USA* **2016**, *113*, 257–261.
[10] B. Abécassis, C. Cottin-Bizonne, C. Ybert, A. Ajdari, L. Bocquet, *New J. Phys.* **2009**, *11*, 075022.
[11] S. W. Joo, S. Y. Lee, J. Liu, S. Qian, *ChemPhysChem* **2010**, *11*, 3281–3290.
[12] M. Wanunu, W. Morrison, Y. Rabin, A. Y. Grosberg, A. Meller, *Nat. Nanotechnol.* **2010**, *5*, 160–165.
[13] J. Diao, L. Young, S. Kim, E. A. Fogarty, S. M. Heilman, P. Zhou, M. L. Shuler, M. Wu, M. P. DeLisa, *Lab Chip* **2006**, *6*, 381–388.

[14] S. Ebbens, D. A. Gregory, G. Dunderdale, J. R. Howse, Y. Ibrahim, T. B. Liverpool, R. Golestanian, *Europhys. Lett.* **2014**, *106*, 58003.
[15] J. R. Howse, R. A. L. Jones, A. J. Ryan, T. Gough, R. Vafabakhsh, R. Golestanian, *Phys. Rev. Lett.* **2007**, *99*, 48102.
[16] L. M. Barge, T. P. Kee, I. J. Doloboff, J. M. P. Hampton, M. Ismail, M. Pourkashanian, J. Zeytounian, M. M. Baum, J. A. Moss, C.-K. Lin, et al., *Astrobiology* **2014**, *14*, 254 – 270.
[17] Y. Ding, B. Batista, O. Steinbock, J. H. E. Cartwright, S. S. S. Cardoso, *Proc. Natl. Acad. Sci. USA* **2016**, *113*, 9182 – 9186.
[18] B. C. Batista, O. Steinbock, *J. Phys. Chem. C* **2015**, *119*, 27045 – 27052.
[19] L. M. White, R. Bhartia, G. D. Stucky, I. Kanik, M. J. Russell, *Mackinawite and Greigite in Ancient Alkaline Hydrothermal Chimneys: Identifying Potential Key Catalysts for Emergent Life*, **2015**.
[20] B. Herschy, A. Whicher, E. Camprubi, C. Watson, L. Dartnell, J. Ward, J. R. G. Evans, N. Lane, *J. Mol. Evol.* **2014**, *79*, 213 – 227.
[21] C. B. Mast, S. Schink, U. Gerland, D. Braun, *Proc. Natl. Acad. Sci. USA* **2013**, *110*, 8030 – 8035.
[22] C. B. Mast, D. Braun, *Phys. Rev. Lett.* **2010**, *104*, 188102.
[23] M. Kreysing, L. Keil, S. Lanzmich, D. Braun, *Nat. Chem.* **2015**, *7*, 203 – 208.
[24] D. Rickard, I. B. Butler, A. Oldroyd, *Earth Planet. Sci. Lett.* **2001**, *189*, 85 – 91.
[25] V. Sojo, A. Pomiankowski, N. Lane, *PLoS Biol.* **2014**, *12*, e1001926.
[26] D. C. Prieve, R. Roman, *J. Chem. Soc. Faraday Trans. 2* **1987**, *83*, 1287.
[27] T.-Y. Chiang, D. Velegol, *J. Colloid Interface Sci.* **2014**, *424*, 120 – 123.
[28] A. Yamaguchi, M. Yamamoto, K. Takai, T. Ishii, K. Hashimoto, R. Nakamura, *Electrochim. Acta* **2014**, *141*, 311 – 318.
[29] K. Punia, M. Bucaro, A. Mancuso, C. Cuttitta, A. Marsillo, A. Bykov, W. L'Amoreaux, K. S. Raja, *Langmuir* **2016**, *32*, 8748 – 8758.
[30] A. Kar, R. Guha, N. Dani, D. Velegol, M. Kumar, *Langmuir* **2014**, *30*, 793 – 799.

Manuscript received: November 4, 2016
Revised: January 9, 2017
Final Article published: January 24, 2017

